

Photoluminescent electrospun fibrous mats for UV detector cards

M. Navarrete^a, J. Gutiérrez^a, R. Mayen-Mondragon^b, D. Aguirre-Aguirre^c, and J. Naude^d

^aLab. Pruebas No Destructivas, Instituto de Ingeniería.

^bGrupo de electroquímica y corrosión computacional,

^cLaboratorio de Instrumentación y Metrología Óptica, Polo Universitario de Tecnología Avanzada, UNAM,
Vía de la Innovación 410, PIIT-Monterrey,

Autopista Monterrey- Aeropuerto Km 10. Apodaca, N.L. 66629, México.

^dFacultad de Ingeniería, Universidad Nacional Autónoma de México,
Circuito Exterior S/N, CU, 04510 CDMX, México.

mnm@pumas.iingen.unam.mx

Received 5 September 2019; accepted 25 November 2019

The present paper describes the implementation of the electrospinning technique to manufacture (polymeric-nonwoven) fibrous-mats (with micrometric/nanometric fibers) as photosensitive regions. These mats are tailored and assembled in UV-A radiation detection cards. The selective photoluminescence of our mats is due to the Europium ions (Eu^{3+} , Eu^{+2}) added as Europium nitrate to a polymethyl methacrylate (PMMA) matrix. The electrospinning-equipment operation-parameters such as applied voltage (10 kV), distance from needle tip to collector plate (17 cm), and precursor-solution flow-rate (0.45 mL/h) are determined from the solution of a one-dimensional model comprising three differential equations. The manufactured photoluminescent mats average-fiber-diameter is $1.3 \pm 0.5 \mu\text{m}$, with 76% void volume, average void-size of $7 \mu\text{m}$, and average thickness of $350 \mu\text{m}$. The photoluminescent mats sustain significant light absorption in the wavelength range of 245 to 350 nm and corresponding emission in the visible range of 400 to 650 nm.

Keywords: Electrospun membranes; photoluminescence; detection UV-A radiation; lanthanides.

Se describe la implementación de la técnica de electrohilado para producir membranas fibrosas (no tejidas poliméricas, con diámetros del orden micro-nano-métricas) como áreas de detección sensibles a la luz. Estas membranas son confeccionadas y ensambladas en tarjetas de detección de radiación en el intervalo UV-A. La foto-luminiscencia selectiva se debe a los iones de Europio (Eu^{3+} , Eu^{+2}) añadidos como nitrato de Europio a una matriz de poli (metil-metacrilato) (PMMA). Los parámetros de operación del equipo de electrohilado como: el voltaje aplicado (10 kV), la distancia desde la punta de la aguja hasta la placa colector (17 cm) y el caudal de la solución precursora (0.45 ml/h), se determinan a partir de la solución de un modelo unidimensional que comprende tres ecuaciones diferenciales. Las membranas foto-luminiscentes tienen un diámetro medio de fibra de $1.3 \pm 0.5 \mu\text{m}$, con un volumen de huecos del 76%, un tamaño de huecos promedio de $7 \mu\text{m}$ y un espesor promedio de $350 \mu\text{m}$. Las membranas foto-luminiscentes tienen un intervalo de absorción de 245 a 350 nm y su emisión correspondiente en el intervalo visible de 400 a 650 nm.

Descriptor: Membranas electrohiladas; fotoluminiscencia; detección de radiación UV-A; lantánidos.

PACS: 81.05Lg; 78.55.Kz; 78.40.Me

1. Introduction

The emission of light by chemical compounds or materials is derived from two different mechanisms: incandescence (black body emission) and luminescence. The former does not depend on the chemical nature of the material but only on its temperature, while the latter implies quantum levels [1]. Luminescence is stimulated by different means: Thermal (thermoluminescence), which releases photonic energy trapped in defects; Optical (photoluminescence); Electrical (electroluminescence) and Chemical (bioluminescence). The present paper emphasis is set exclusively on photo-luminescence due to the f-f transitions. Luminescence can be further classified according to the emission mechanism: the fast phenomenon fluorescence, and the slow emission phosphorescence. Lanthanide ions show fluorescence, phosphorescence and often both of them [2].

Continuous electrospinning is a technique that allows the fabrication of one-dimensional micro/nano structures.

Electrospinning comprises an electro-hydrodynamic process where a drop of hanging liquid of a precursor solution at a nozzle exit is electrically charged. The effect is the drop stretching and elongation, resulting in a jet that forms a long fiber. The fiber is then collected on a substrate plate (Fig. 1a). Polymer-based electrospun membranes have become popular as their physical and chemical properties can be easily modified offering greater selectivity. In this direction, fibers with conjugated polymers [3] are being prepared for components such as quantum dots [4,5]. The most common polymers used are: polyvinylpyrrolidone (PVP) [6], polymethylmethacrylate (PMMA) [7], polystyrene (PS) [8], among others. Further mixing with lanthanide ions leads to luminescent properties with defined emission bands, long lifetimes and good quantum efficiency. This has paved the way for other applications such as light-emitting diodes, color screens, lasers and data storage [9]. The main control parameters of the electrospinning-apparatus are the applied electric voltage V [kV], the distance from the tip to the collector

TABLE I. Lanthanide/polymer nanofibers with photo-luminescent properties. V = applied electric voltage, L = tip-to-collector distance, ϕ = fiber diameter, E_x = excitation wavelength, E_m = emission wavelength.

Lanthanide/polymer	V [kV]	L [cm]	ϕ [nm]	E_x [nm]	E_m [nm]	Ref.
GdVO ₄ :Ln ³⁺ /PVP (Ln= Eu, Dy, Sm)	13	17	230-460	276	484, 574, 567 604, 620, 649	[6]
CaWO ₄ :Tb ³⁺ /PVP	15	16.5	120-150	249	416, 545	[7]
β -Ga ₂ O ₃ :Tb ³⁺ /PVP	23	22.5	100-300	325	491, 550 591, 625	[8]
Ln(C ₅ H ₇ O ₂) ₃ /TiO ₂ /PVP Ln=(Er, Ce, Pr)	15	12	200-250	300-400	695, 680, 420	[9]
SiO ₂ :xTb ³⁺	20	20	142-993	229	446, 486, 542 584, 619	[10]

TABLE II. Luminescent composites made of electrospun polymer fibers with Europium and Europium complex.

Europium/polymer	V [kV]	L [cm]	ϕ [nm]	E_x [nm]	E_m [nm]	Ref.
Eu(NO ₃) ₃ / PMMA	12	15	350-400	488	581,592,614, 649, 678	[11]
Eu(TTA) ₃ (TPPO) ₂ / PMMA	14	30	1400	355	613.2	[12]
PS	18	25	800	355	612.3	
PVP	13	25	700	355	614.3	
Eu complex(TTA) ₃ Phen /PMMA	20	15	500-900	350	571, 592, 609.5	[13]
/PS	20	15	300-500	350	612.5	
/PVdF	20	15	200-300	350	579, 589.6, 615.6	
Eu(DBM) ₃ Phen/PS	10	20	300	366	580, 590, 612 653, 705, 802	[14]

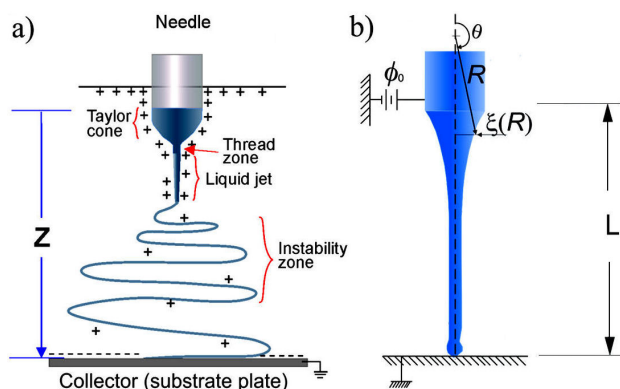


FIGURE 1. a) Schematic diagram of the electrospinning technique showing the tip-to-collector-plate distance (L); b) Configuration coordinates and Taylor's jet dimensions. Main parameters are high voltage DC or AC, (V) and jet radius (R).

L [cm], and the flow rate of the liquid solution [ml/hr]. The main resulting-fiber characteristics are its diameter ϕ , and luminescent properties (band excitation wavelength E_x and band emission wavelength E_m , quantum efficiency, etc.)

Electrospun polymer fibers doped with lanthanides (Ln) such as Erbium, Europium, Terbium, Samarium, Cerium, Dysprosium and Praseodymium with potential for optoelec-

tronic devices, can be found in the literature, Table I. Among them, the trivalent Europium ion stands out due to its intrinsic quantum efficiency [6]. Table II show the characteristics of Europium/polymer electrospun matrices.

This paper presents both theoretical and experimental aspects to produce UV-A detection cards using a unidirectional model, the electrospinning technique, and the optical properties of a Europium lanthanide within a PMMA polymer matrix.

1.1. Europium

Europium ions (II, III) belong to the lanthanides having an absorption band of 200 to 400 nm and an emission band in the visible range of (400-780) nm. In general, the efficiency of the trivalent-lanthanide-ion surroundings to sensitize the material luminescence is a key parameter in the design of highly emitting molecular structures and materials.

2. Model

The electrospinning process can be simulated via a quasi-unidirectional model [15]. The model results can then be

used to specify the electrospinning-equipment control parameters. The model considers an electro-hydro-dynamically-driven capillary jet with negligible charge relaxation effects, *i.e.* when a Taylor's charged capillary jet is formed under steady state regime. In terms of characteristic times, the electrical relaxation time $\beta\varepsilon_0/K$ is small compared to the hydrodynamic residence time of a liquid particle within the jet $t_0 \sim l/U \sim LR_j^2/Q$, where β is the liquid to vacuum electrical permittivity ratio, K is the electrical conductivity, L and R_j are spatial coordinates (Fig. 1b) referring to jet length and jet diameter. U and Q are the axial velocity and liquid flow rate, respectively. Most important is that at equilibrium the inner electric field is zero [16].

The one-dimensional model comprising the equations of mass-, momentum- and charge conservation and the condition of the capillary [15] is defined by:

$$v = \frac{Q}{\pi\xi^2}, \quad (1)$$

$$\frac{\xi}{2\varepsilon_0} \frac{d}{dz} \left(p + \frac{1}{2}\rho v^2 \right) = E_n^0 E_z, \quad (2)$$

$$I = \frac{2Q\varepsilon_0}{\xi} E_n^0 + \pi\xi^2 K E_z, \quad (3)$$

$$\frac{\gamma}{\xi} = p + \frac{\varepsilon_0}{2} ((E_n^0)^2 + (\beta - 1)E_z^2), \quad (4)$$

where: Z -Axial coordinate, ξ -Jet radius, p -Pressure drop, v -Liquid velocity, γ - Liquid surface tension, I -Total electric current, K -Electrical conductivity, ρ -Liquid density, Q -Flow rate, E_n^0 -Electric field normal component, E_z -Electric field tangential component at the jet's surface, ε_0 -Vacuum permittivity.

The above Eqs. (1-4) are reduced to a first order ordinary differential equation for E_n^0 Eq. (5), which itself requires the determination of $d\xi/dz$ and dP/dz , Eqs. (6) and (7):

$$\frac{dE_n^0}{dz} = \frac{\left[\frac{\gamma}{\xi^2} - \frac{2(\beta-1)\varepsilon_0 I^2}{\pi^2 K^2 \xi^5} - \frac{12(\beta-1)Q^2 \varepsilon_0^3}{\pi^2 K^2 \xi^7} (E_n^0)^2 + \frac{10(\beta-1)Q\varepsilon_0^2 I}{\pi^2 K^2 \xi^6} E_n^0 + \frac{2\rho Q^2}{\pi^2 \xi^5} \right] \frac{d\xi}{dz}}{\frac{2Q\varepsilon_0^2 I(\beta-1)}{\pi^2 K^2 \xi^2} - \left[\varepsilon_0 + \frac{4(\beta-1)Q^2 \varepsilon_0^3}{\pi^2 K^2 \xi^6} \right] E_n^0} + \frac{\frac{2\varepsilon_0 E_n^0}{\pi \xi^3 K \left(I - \frac{2Q\varepsilon_0}{\xi} E_n^0 \right)}}{\frac{2Q\varepsilon_0^2 I(\beta-1)}{\pi^2 K^2 \xi^5} - \left[\varepsilon_0 + \frac{4(\beta-1)Q^2 \varepsilon_0^3}{\pi^2 K^2 \xi^6} \right] E_n^0}, \quad (5)$$

$$\frac{d\xi}{dz} = \frac{4I\varepsilon_0 E_n^0 \xi}{\rho Q K} - \frac{8\varepsilon_0^2 (E_n^0)^2}{\rho Q K} - \frac{2\pi\xi^4}{\rho Q^2} \left(\frac{dP}{dz} \right), \quad (6)$$

$$\frac{dP}{dz} = \frac{2Q^2}{\pi\xi^5} \left(\frac{d\xi}{dz} \right) + \frac{2\varepsilon_0 E_n^0 (I - 2Q\varepsilon_0 E_n^0 \xi)}{\pi\xi^3 K}. \quad (7)$$

The characteristic jet radius, axial length, and normal and tangential components of the initial electric field can be determined from:

$$\varepsilon_0 (E_{n0}^0)^2 \sim \frac{\rho Q^2}{R_0^4}, \quad (8)$$

$$\frac{\rho Q^2}{(R_0^4)} \sim \frac{\varepsilon E_{no}^0 E_{zo}}{R_0}, \quad (9)$$

$$\frac{\varepsilon_0 Q E_{n0}}{R_0} \sim R_0^2 K E_{z0}. \quad (10)$$

Using the corresponding physical parameters of the precursor solution, the following initial conditions can be calculated:

$$Q_0 = \frac{\gamma\varepsilon_0}{\rho K}, \quad (11)$$

$$I_0 = \varepsilon_0^{1/2} \gamma \rho^{-1/2}, \quad (12)$$

$$d_0 = (\pi^{-2} \gamma \varepsilon_0^2 \rho^{-1} K^{-2})^{1/3}, \quad (13)$$

$$E_0 = (2\gamma\varepsilon_0^{-1} d_0^{-1})^{1/2}. \quad (14)$$

The liquid flow rate Q dependence with Z is calculated with:

Jet area:

$$A = \pi [(\sqrt{Z^2 + (R_0 - r)^2}) * (R_0 + r)R_0^2 + r^2], \quad (15)$$

Evaporation time:

$$t_{\text{evap}} = \bar{R} * A, \quad (16)$$

Evaporation rate:

$$V_{\text{evap}} = \frac{Z}{t_{\text{evap}}}, \quad (17)$$

$$Q = V_{\text{evap}} * A,$$

Thus:

$$Q(z) = \frac{z\pi R_0^2}{R * \{ \pi [(\sqrt{z^2 + (R_0 - r)^2}) * (R_0 + r) + R_0^2 + r^2] \}}. \quad (18)$$

Considering the figures of merit derived from the previous equations solution, an electrospinning flow rate Q can be selected that guarantees the solvent evaporates within the path from capillary to collector (Fig. 1b).

3. Experimental

Reagents:

Polymethylmethacrylate (PMMA), CAS 9011-14-7, MW = 120000 g/mol, density 1.17 g/ml, purity 95-99%, $T_g = 85 - 165^\circ\text{C}$, flash point 250°C , auto-inflammation 304°C .

Dimethylformamide (DMF), CAS 68-12-2, MW = 73.09 g/mol, density 0.944 g/cm^3 , purity 99.8%, melting point 61°C , boiling point 153°C , viscosity 0.92 cP at 20°C .

Europium (III) nitrate pentahydrate ($\text{EuN}_3\text{O}_9 \cdot 5\text{H}_2\text{O}$) CAS 63026-01-7, MW = 428.06 g/mol, Purity 99.9%.

Precursor solution:

The first solution is prepared dissolving 0.7 g of poly (methyl methacrylate) (PMMA) powder in 15 ml of N, N-dimethylformamide (DMF). A second solution is then prepared dissolving 105.8 mg of EuN_3O_9 in 5 ml of DMF. The second solution is added to the first one and the resulting mixture is stirred in a thermal bath at around 40°C . PMMA is then very slowly added to the mixture until a total amount of 7.54 g (the last step took almost six hours). The final solution is labeled as “precursor”.

Physical characterization of PMMA/DMF solution:

The precursor solution density ($1.02\text{ [g/cm}^3\text{]}$) was determined with a pycnometer (Kimble Chase Kimax). The electrical conductivity (5.6 [mS/cm]) was determined with an EC meter (CL8, Conductronic). The liquid surface tension at the interface with air ($0.0154\text{ [Nm}^{-1}\text{]}$) was determined with a tensiometer (sessile drop, Fanyuan instrument).

DMF evaporation:

An ad hoc experiment is conducted to measure the time required by a thin film of solvent (with known surface area) laying on a PMMA sheet to fully evaporate. This is the average solvent-evaporation-time. At our laboratory conditions an average evaporation rate of $\bar{R} = t_{\text{evapDMF}}/A_{\text{DMF}} = 1.96\text{ s/mm}^2$ is determined.

4. Simulation

Equations (5-7) are solved applying the Runge-Kutta method within the Matlab environment. The initial conditions considered are $\xi = 2\text{ mm}$; $P = 78\text{ kPa}$; $Z(0) = 0\text{ m}$. The electric field was varied from 5 to 18 kV. Figure 2 shows the electric-field normal-component drop as a function of the axial coordinate Z . The figure helps identify the maximum distance between needle and collector plate at which electrospinning is still possible, L , according to the initially applied voltage.

Flow rate Q dependence with $Z(L)$

Figure 3 shows the required precursor-solution flow-rate Q as a function of the distance from the tip to the collector plate Z and the average solvent-evaporation-rate. The model input parameters are needle radius 0.4 mm , and final fiber radius $0.5\text{ }\mu\text{m}$. As an example, considering an evaporation rate of 3.92 s/mm^2 , Q must be around 0.4 ml/h for every practical Z .

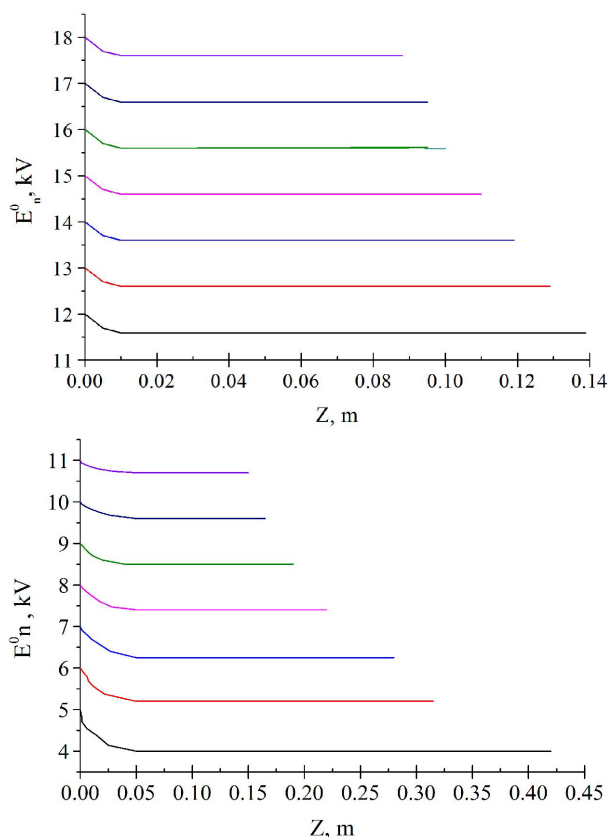


FIGURE 2. Electric-field normal-component drop as a function of the axial coordinate Z and initial field, keeping all other parameters constant.

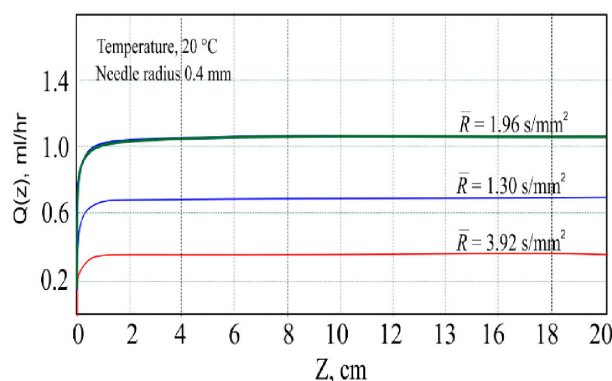


FIGURE 3. Precursor-solution flow-rate Q at different evaporation rates, \bar{R} . We consider the fiber falling down in a straight line to the collector plate. The fiber thins along the way until a terminal diameter, $2r$.

5. Electrospun mat design

The results of the one-dimensional-model calculations can help define an experimental work-region where good fiber formation is attained, Fig. 4. It is a visual representation of the recommended working range of the most significant experimental control-parameters: distance between electrodes,

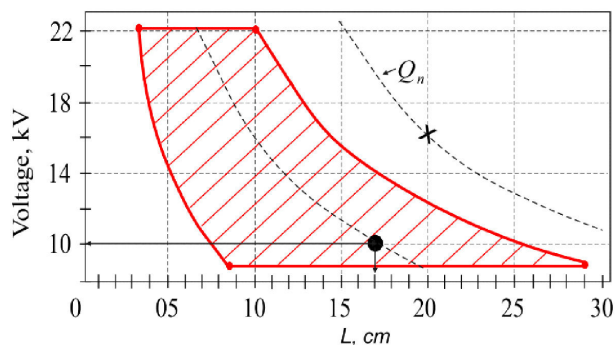


FIGURE 4. Recommended work-region to attain good-quality electrospun mats. The main control parameters are applied voltage, distance between electrodes, and precursor solution flow rate (Q).

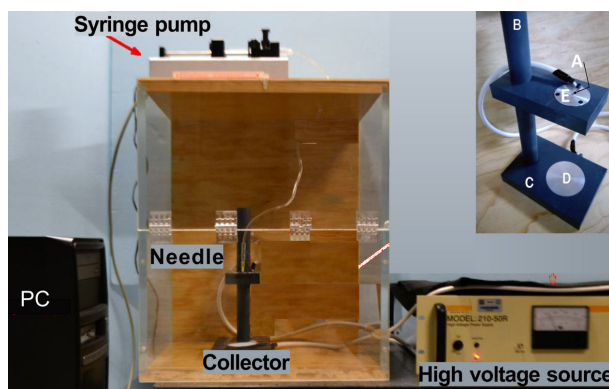


FIGURE 5. Electrospinning apparatus showing its main modules with labels. Inset shows, the components that support the electrodes: (A) capillary position to feed the flow rate; (B) is the electrodes-separation-distance adjustment-rod; (C) is the fix plate. (D) and (E) are aluminum electrodes.

applied voltage and precursor-solution flow rate, and the rest of the parameters are constant.

5.1. Electrospinning

An image of our homemade electrospinning apparatus is shown in Fig. 5.

5.2. Preparation of the PMMA/DMF electrospun mats

The first electrospinning tests performed were to prove the validity of our model-predicted work-region (Fig. 4). Thus, a sample of the PMMA/DMF solution is electrospun with values for applied-voltage, distance-between-electrodes, and precursor-solution flow-rate located within the recommended work-region. Our first fibers were attained with a voltage of 16 kV, $L = 20$ cm. And flow rate of 0.65 ml/hr. Several tests afterwards, we were able to fabricate outstanding mats with 10 kV, 0.45 ml/hr, and 17 cm. A photograph of such an electrospun PMMA-mat is shown in Fig. 6a. Figure 6b is Scanning Electron Microscopy micrograph of the mat, showing fiber size and arrangement. Table III presents the main physical characteristics of the mats.

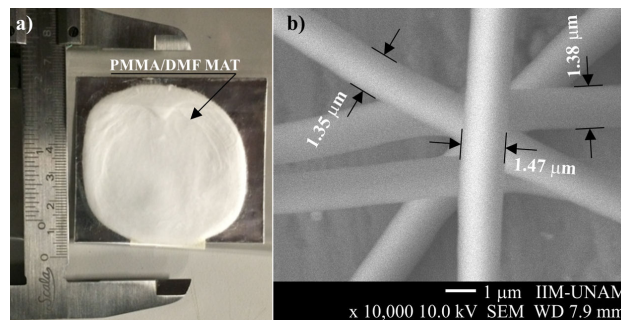


FIGURE 6. Successfully-electrospun PMMA/DMF mat images. a) Sample size; b) Scanning electron microscopy micrograph showing fiber size and arrangement.

TABLE III. Physical characteristics of the PMMA electrospun mats.

Mat #	Area [mm ²]	Weight [g]	Thickness [mm]	Density [Kg/m ³]
1	1179.09	0.243	0.69	2994
2	1594.42	0.256	0.58	2853
3	1905.05	0.153	0.26	3097
4	604.81	0.082	0.30	4520
5	951.46	0.086	0.33	2749

5.3. Preparation of the PMMA/DMF/Europium-ion electrospun composites

As our goal was to fabricate electrospun mats that could absorb electromagnetic radiation in the UV range and emit in the visible range (for human eye detection), we added to the polymer matrix EuN3O9, in a concentration of 2% w/w. That is, 105.8 mg of Europium nitrate per 20 ml of the 30% w/w of PMMA/DMF solution.

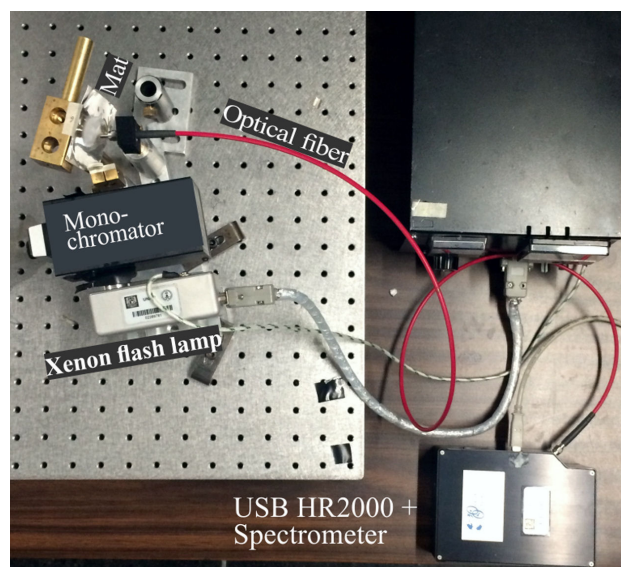


FIGURE 7. Optical arrangement for the optical characterization of fibrous luminescent mats.

5.4. Optical and morphological characterization of the fibrous luminescent mats

The optical arrangement to evaluate the optical properties of the fabricated mats is shown in Fig. 7. A Xenon flash lamp (Hamamatsu) is the incident-light source. The light beam is

forced to travel through a mini-monochromator (Oriel, 240-800 nm) and a quartz lens (5 cm focus) in its way towards the sample. The arrangement allows generating light pulses from 240 to 350 nm. Fourier transform UV-VIS spectra are captured using a quartz optical fiber connected to a spectrometer

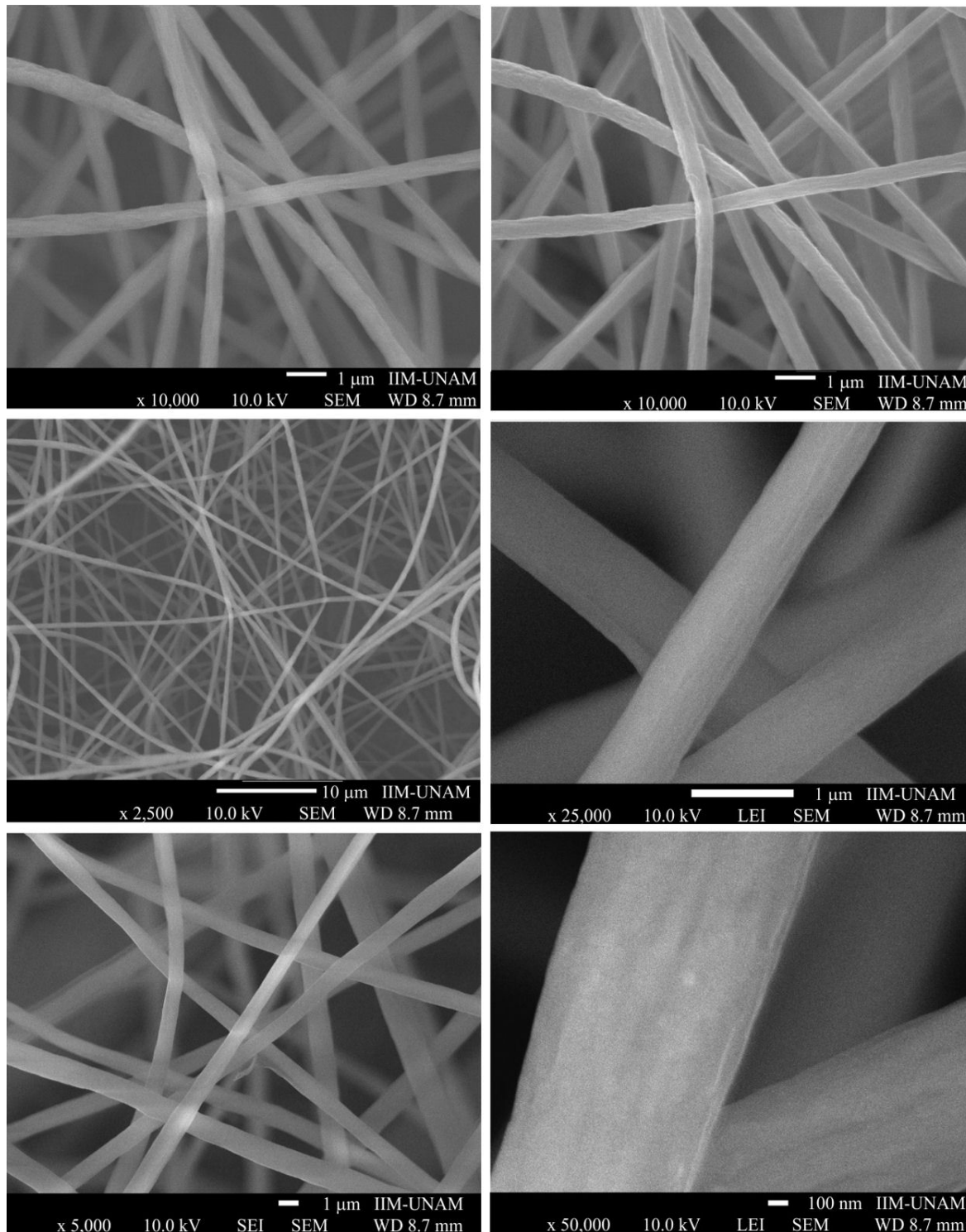


FIGURE 8. Scanning Electron Microscopy images of the electrospun microfiber-luminescent-mats at different scales. Image at the bottom right, is a zoom-in to distinguish the fiber texture.

using a quartz optical fiber connected to a spectrometer (Ocean Optics USB HR 2000+). The morphological characterization of the fibrous mats was performed with the aid of a Scanning electron microscope (SEM; JEOL 7600).

6. Results

6.1. Morphology of the fibrous luminescent mats

SEM images, at different scales, of a luminescent electrospun mat are shown in Fig. 8. The long fibers appear randomly arranged. Relatively long segments of uniform diameter can be found. The transition between segments of different diameter is continuous. Analyzing the SEM images with the aid of the Image J software, we find an average fiber-diameter of $1.4 \mu\text{m}$, filling mat volume of 24% and gap average-size of $7 \mu\text{m}$. The doping material seems to be fully contained within the fiber.

6.2. Optical response

Figure 9 shows an image of the luminescent response at an optically excited spot of the electrospun mat. The color is characteristic of the Eu^{3+} ion. In our fabricated samples, the emission wavelength peaks at around 612 nm. Figure 10 shows the spectroscopic response of the electrospun mat according to the selected incident-wavelength of the Xenon-flash-lamp source. The emission band profile presents visible-peak displacements and peak-intensity variations. This is due to the heterogeneous composition and morphology of the mat. Different regions with different optical activity (due to variations in the europium ion environment within the PMMA matrix) respond in a different way to the incident excitation band.

Figure 11 shows the spectroscopic response of the assembled UV-A detection card, with overall dimensions of 80×50 mm. The photosensitive mat, on the top of the card (30-gauge white styrene sheet), measures 20×35 mm; absorption and emission profiles are printed in the adjoining area. The card is protected between PMMA thin films. Emission band shows the two main peaks at 525 nm and 612 nm.



FIGURE 9. Image of the luminescence displayed by the electrospun mat where a UV light spot strikes. $E_x = 250 \text{ nm}$, $E_m \approx 612 \text{ nm}$.

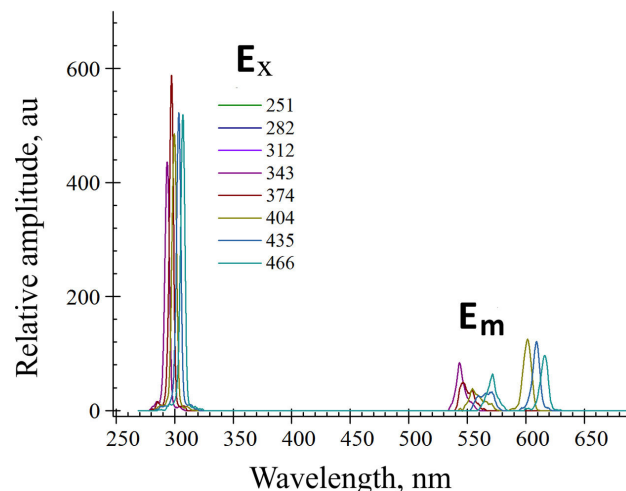


FIGURE 10. Spectroscopic response of the electrospun mat according to the incident excitation band (250 to 360 nm).

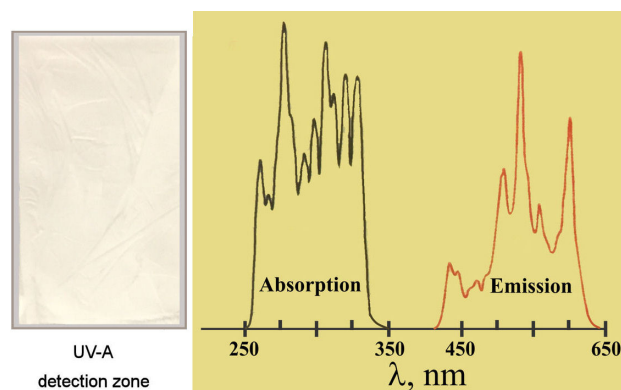


FIGURE 11. UV-A detection card assembled. Left; UV-A photosensitive region (electrospun PMMA / DMF / Europium mat), right; profiles of UV absorption (sensitivity curve) and emission response in the visible band.

7. Discussion and conclusions

In the present paper, a methodology was developed to successfully produce electrospun fibrous-mats with photoluminescent characteristics. The mats are used as a photosensitive material on viewing cards tailored to operate in the UV-A absorption wavelength range.

According to the SEM-image observations, the Europium ions remain fully contained within the fiber (there are no crystals outside the fibrous web). This is advantageous, as any crystals outside the polymer matrix could be washed out of the mat during further processing.

The solution of the equations from the implemented one-dimensional-model helped define a set of recommended working ranges of the main experimental control-parameters: applied voltage, distance between electrodes and precursor solution flow rate. Working with such set of values is recommended to attain a good mat quality. Moreover, sweeping the experimental parameters within such work-region allows

optimizing the fabrication conditions and thus enhancing the mat properties. Most of the published manuscripts dealing with the electrospinning process, for a specific application, do not report how the experimental fabrication parameters were derived. In many cases, such parameters are only slight modifications of conditions previously reported (concentrations, flow rate, distance between electrodes and mean fiber diameter). It must not be forgotten, that for the electrospinning technique, it is necessary to fully specify such operational parameters, as shown in Table I. Even when our fabrication methodology led to enhanced-quality mats, we did not in general attain the final fiber-diameter sought. Diameters less than one micron were only found on certain specific segments of the mat-fiber. We thus need, to further modify our model by integrating additional parameters, which were not considered or to perform a more thorough experimental characterization of our precursor solution. For example, we did not consider the electrical conductivity variation of the precursor solution caused by adding the Europium salt. In any

case, our results are in good agreement with the published literature [11].

Regarding the mat optical properties, the emission spectra displacement according to the selected excitation wavelength, generates the possibility of fabricating wavelength-specific UV detector cards. To this end, it is however necessary to improve the mat resistance to mechanical loads and to increase its water-resistance, since they are still fragile and absorb an undesired amount of water from environment [17]. Thus, we are looking forward to attain larger filling volumes and to reduce the average gap-size of the mat.

Acknowledgments

The present work is supported financially by the PAPIIT-UNAM (Programa de apoyo a proyectos de investigación Tecnológico), IN106919: Study of the cavitation and embolism process in vascular plants.

-
1. E. Newton Harvey, *A History of Luminescence*. From the Earliest Times until 1900, The American Philosophical Society, Philadelphia, (1957) 1-7.
 2. J.-C.G. Bünzli, and S.V. Eliseeva, in: O.S. Wolfbeis, M. Hof (Eds.), Springer Series on Fluorescence. *Lanthanide Luminescence: Photophysical, Analytical and Biological Aspects*, vol. 7, Springer Verlag, Berlin, (Chapter 7) (2011) p. 1-45.
 3. S. Agarwala, A. Greinera, and J. H. Wendorff, *Prog. Polym. Sci.* **38** (2013) 963-991.
 4. T. Abitbol, J. T. Wilson, and D. G. Gray, *J. Appl. Polym. Sci.* **119** (2011) 803-10.
 5. A. Rosendo, M. Flores, G. Córdoba, R. Rodríguez, and R. Arroyo, *Mater. Lett.* **57** (2003) 2885-2893.
 6. X. Li *et al.*, *J. Solid State Chem.* **184** (2011) 141-148.
 7. H. Liang, F. Xie, X. Ren, Y. Chen, B. Chen, and F. Guo, *Spectrochim. Acta A* **116** (2013) 317-320.
 8. H. Zhang *et al.*, *J. Phys. Chem. C* **112** (2008) 9155-9162.
 9. H. Wang, Y. Wang, Y. Yang, X. Li, and C. Wang, *Mater. Res. Bull.* **44** (2009) 408-414.
 10. M.M.A. Abualrejal, H. Zou, J. Chen, Y. Song, and Y. Sheng, *Advances in Nanoparticles* **6** (2017) 33-47.
 11. M. Li *et al.*, *Mater. Res. Bull.* **47** (2012) 321-327.
 12. H. Zhang *et al.*, *J. Phys. Chem. C* **112** (2008) 9155-9162.
 13. M. P. Dandekar, S. B. Kondawar, S. G. Itankar, and D. V. Nandanwar, *Procedia Materials Science* **10** (2015) 80-587.
 14. L. Huang *et al.*, *Opt. Commun.* **285** (2012) 1476-1480.
 15. A. M. Gañán-Calvo, *J. Fluid Mech.* **335** (2010) 165-188.
 16. R. F. Probstein, *Physicochemical Hydrodynamics*, An introduction. Butterworth-Heinemann, (1989).
 17. M. Navarrete *et al.*, *Int. J. Thermophys.* **38** (2017) 121-133.